Research Square

Preprints are preliminary reports that have not undergone peer review.
They should not be considered conclusive, used to inform clinical practice,
or referenced by the media as validated information.

Penetration Electric Fields and Disturbance Dynamo Effects During the November 2025 Geomagnetic Storm

Efrem Amanuel Data

immanuelefawu@gmail.com

Wolaita Sodo University

Emmanuel Duadi Sulungu

University of Dodoma

Gebre Kalute Gebino

Wolaita Sodo University

Research Article

Keywords: Geomagnetic storm, TEC, EEJ, GNSS, disturbance dynamo electric field

Posted Date: February 27th, 2026

DOI: https://doi.org/10.21203/rs.3.rs-8971002/v1

License: This work is licensed under a Creative Commons Attribution 4.0 International License.
Read Full License

Additional Declarations: No competing interests reported.

Penetration Electric Fields and Disturbance Dynamo Effects During the November 2025 Geomagnetic Storm

Efrem Amanuel Data[a,*], Emmanuel Daudi Sulungu[b], and Gebre Kalute Gebino[a]

[a]Department of Physics, Wolaita Sodo University, Ethiopia
[b]Department of Physics, The University of Dodoma, Tanzania
[*]Corresponding Author: immanuelefawu@gmail.com

Abstract

The November 2025 geomagnetic storm generated pronounced perturbations in the equatorial and low-latitude ionosphere through enhanced magnetosphere–ionosphere–thermosphere coupling. This study quantifies the relative contributions of prompt penetration electric fields (PPEFs) and disturbance dynamo electric fields (DDEFs) in regulating storm-time electrodynamics across multiple longitudinal sectors, including Africa, South America, and Southeast Asia. GNSS-derived total electron content (TEC) data from six IGS stations, ground-based magnetometer measurements from two stations, and solar wind, thermospheric O/N_2 ratio, and geomagnetic indices (Dst, Kp, V_{sw}, E_y, IMF) were employed to characterize the ionospheric response. Results show that PPEFs dominate the storm main phase, producing rapid eastward plasma drifts, intensified equatorial electrojet (EEJ), and TEC enhancements up to $\sim 80\%$ above quiet-time levels. Conversely, DDEFs emerge during the recovery phase, generating westward electric fields that suppress TEC and weaken or reverse EEJ signatures. Spatial analysis reveals significant longitudinal and latitudinal asymmetries, reflecting regional geomagnetic configurations, background ionospheric conditions, and storm-driven thermospheric wind dynamics. These findings highlight the sequential and competing roles of PPEFs and DDEFs in shaping storm-time equatorial and low-latitude ionospheric variability, emphasizing the necessity of incorporating both mechanisms into ionospheric forecasting frameworks to improve GNSS performance and mitigate space weather impacts.

Keywords: Geomagnetic storm, TEC, EEJ, GNSS, disturbance dynamo electric field

1 Introduction

Geomagnetic storms are among the most profound drivers of space weather disturbances in the near-Earth environment (Mannucci and Tsurutani, 2017; Malik et al., 2010). These storms originate from enhanced energy and momentum injection into the Earth's magnetosphere following solar eruptive events such as coronal mass ejections (CMEs) and high-speed solar wind streams (Pierrard et al., 2025; Burton et al., 1975). A sustained southward turning of the interplanetary magnetic field (IMF) facilitates magnetic reconnection at the dayside magnetopause, enhancing magnetospheric convection and driving substantial geomagnetic disturbances at Earth (Daglis et al., 1999; Gonzalez et al., 1994). This process leads to a dramatic reconfiguration of current systems, including the ring current, field-aligned currents, and auroral electrojets, manifesting as the characteristic depression in the Dst (disturbance storm time) index during storm main phases (Dungey, 1961; Luo et al., 2026). Among these, storm-time electric fields play a central role in modulating plasma dynamics

in the ionosphere, particularly at low and equatorial latitudes where background electric fields and neutral winds dominate quiet-time behavior (Sulungu, 2024; Seba and Nigussie, 2016). The ionosphere responds to storm-induced perturbations primarily through PPEFs and DDEFs, which have contrasting physical origins and temporal characteristics but collectively govern storm-time electrodynamics (Tsurutani, 2008; Fejer et al., 2024). Prompt penetration electric fields arise directly from changes in magnetospheric convection electric fields following enhanced solar wind forcing. During the onset and main phase of geomagnetic storms, intensified magnetospheric convection rapidly penetrates to low and equatorial latitudes due to weakened shielding by region-2 field-aligned currents (Dungey, 1961; Kikuchi and Hashimoto, 2016). This process leads to PPEFs that persist for tens of minutes to several hours and are driven by enhanced day-side re-connection and large-scale current systems (Tsurutani, 2008). PPEFs are typically eastward during storm main phases under southward IMF conditions, resulting in enhanced upward E×B plasma drift near the magnetic equator (Lu et al., 2012; Zhang et al., 2025). Conversely, during IMF northward turnings or over shielding intervals, PPEFs may become westward, suppressing or reversing vertical plasma drifts (Kikuchi and Hashimoto, 2016; Tulasi Ram et al., 2019). The immediate consequence of PPEFs is the rapid modification of the EEJ and vertical plasma drifts, which directly regulate the equatorial fountain process and equatorial ionization anomaly (EIA) development (Archana et al., 2023a; Bai, 2025). Eastward PPEFs enhance upward E×B drift, lifting the F-region plasma to higher altitudes where recombination rates are reduced, producing positive ionospheric storm effects characterized by increased TEC (Venugopal et al., 2025; Zhang et al., 2025; Paul, 2025). In contrast, westward PPEFs suppress vertical transport and often result in negative storm effects, marked by TEC depletion (Chen, 2025). These storm-time TEC variations significantly affect radio wave propagation, satellite communication systems, and GNSS positioning accuracy (Sulungu, 2024; Dow et al., 2009). In contrast to the rapid PPEF response, DDEFs develop gradually and persist longer into storm recovery phases. DDEFs originate from storm-induced modifications of thermospheric circulation caused by enhanced auroral Joule heating and particle precipitation (Han et al., 2011; Meier et al., 2005). The resulting equator-ward neutral winds interact with ionospheric plasma in the E-region dynamo layer (90–140 km), generating global-scale electric fields that propagate to low latitudes (Fejer et al., 2024; Lu et al., 2012). Unlike PPEFs, which are externally driven by magnetospheric convection, DDEFs reflect the delayed atmospheric response to geomagnetic forcing and typically emerge 3–6 hours after storm onset (Lu et al., 2012; Zhang et al., 2025). Despite their different physical origins, PPEFs and DDEFs frequently coexist during geomagnetic storms and can act in competing ways. PPEFs often dominate the storm main phase, producing rapid ionospheric uplift and TEC enhancement, whereas DDEFs become increasingly important during late main and recovery phases, driving westward electric fields that suppress the equatorial fountain effect and contribute to negative storm phases (Tsurutani, 2008; Paul, 2025). The relative dominance of these mechanisms determines the overall ionospheric response, producing strong spatial and temporal variability in TEC, vertical drift patterns, and E-region current systems (Bojilova and Mukhtarov, 2024; Yizengaw, 2021). The persistence of DDEFs, which may last more than 24 hours after storm onset, plays a crucial role in altering low-latitude electrodynamics. These fields have been associated with prolonged westward electric fields that counteract quiet-time eastward drifts and suppress the equatorial PRE (Fejer et al., 2024; Pierrard et al., 2025). As a result, DDEFs can inhibit equatorial plasma instability growth and reduce the occurrence of equatorial spread-F and ionospheric scintillation (Tsurutani, 2008; Dow et al., 2009). Such storm-time dynamo effects have been widely documented through magnetometer observations and ionosonde measurements that reveal altered EEJ behavior and sustained TEC depletion during recovery phases (Seba and Nigussie, 2016; Moraes-Santos, 2024). A substantial body of literature has documented global ionospheric responses to PPEFs and DDEFs during major geomagnetic storms. Both observational and

modeling studies have demonstrated that storm-driven electric fields modulate TEC far from auroral source regions, emphasizing the global coupling of magnetospheric forcing and low-latitude electrodynamics (Mannucci and Tsurutani, 2017; Data, 2025). GNSS-derived TEC observations provide high temporal resolution and global coverage, enabling detection of both rapid storm-time TEC enhancements associated with PPEFs and long-duration TEC suppressions related to DDEFs and thermospheric composition changes (Dow et al., 2009; Tulasi Ram et al., 2019). These studies further indicate that storm-time TEC responses depend strongly on local time, season, background ionospheric conditions, and longitudinal sector (Fejer et al., 2024; Seba and Nigussie, 2016). Beyond TEC magnitude variations, PPEFs and DDEFs significantly influence ionospheric irregularity formation. Enhanced PPEFs can intensify post-sunset vertical drifts, triggering Rayleigh–Taylor instabilities that lead to equatorial spread-F and scintillation activity (Sulungu, 2024; Tulasi Ram et al., 2019). Conversely, DDEF-driven westward electric fields and altered thermospheric winds can suppress instability growth, modifying the spatial distribution and occurrence rate of scintillation events (Fejer et al., 2024; Dow et al., 2009). This complex interaction highlights the critical role of storm-time electric fields in shaping ionospheric structure and radio propagation conditions. Although extensive storm-time electrodynamic studies exist for American and Pacific longitude sectors, comparatively fewer investigations have focused on African and Indian equatorial regions due to limited ground-based instrumentation (Seba and Nigussie, 2016; Yizengaw, 2021). Nevertheless, available case studies over Africa confirm that PPEFs and DDEFs produce similar electrodynamic signatures, including modified EEJ intensity and storm-phase-dependent TEC responses (Seba and Nigussie, 2016; Sulungu, 2024). These findings emphasize the importance of regional investigations and motivate further analysis of major events such as the November 2025 geomagnetic storm within the Africa, South America, and Southeast Asian sectors (Pulinets, 2026). The November 2025 geomagnetic storm therefore provides a valuable opportunity to examine the competing roles of PPEFs and DDEFs over East Africa. This study aims to quantify the relative contributions of penetration electric fields and disturbance dynamo effects to ionospheric electrodynamics during this event. Using combined GNSS TEC observations and ground-based magnetometer measurements, this work seeks to clarify how storm-time electric fields regulate plasma transport, TEC enhancement or depletion, and equatorial current systems within an underrepresented longitudinal sector.

2 Data and Methods

This study investigates the dominant electrodynamic drivers controlling ionospheric variability during the November 2025 geomagnetic storm by integrating geomagnetic indices, solar wind and IMF parameters, ionospheric TEC, and ground-based magnetometer measurements. Such multi-instrument approaches are widely adopted to characterize storm-time magnetosphere–ionosphere coupling and to distinguish prompt penetration electric field (PPEF) signatures from disturbance dynamo electric field (DDEF) effects (Gonzalez et al., 1994; Fejer et al., 2024; Fuller-Rowell et al., 1994). Standardized data repositories and established processing techniques were employed to ensure reproducibility and consistency with prior storm-time ionospheric investigations.

2.1 Geomagnetic and Solar Wind Parameters

To characterize magnetospheric forcing and derive storm-time electrodynamic drivers, the following parameters were used:

Dst Index: The Dst index was used as a proxy for ring current intensity and storm main-phase development. Hourly Dst data were obtained from the World Data Center for Geomagnetism, Kyoto

University. The Dst index quantitatively reflects the globally averaged depression of the horizontal magnetic field at low latitudes due to enhancement of the ring current. Physically, a negative Dst corresponds to increased magnetospheric energy storage in trapped particle populations (Burton et al., 1975; Sckopke, 1966).

Planetary Kp Index: The 3-hour planetary Kp index was used to classify storm phases and assess global geomagnetic disturbance levels (Menvielle, 2013). Kp represents mid-latitude magnetic activity and provides a global indicator of geomagnetic variability.

Solar Wind and IMF Parameters: High-resolution (1-min and 5-min) solar wind plasma parameters and IMF components (B_x, B_y, B_z), solar wind speed ($V_{\rm sw}$), and interplanetary electric field (IEF) were obtained from the NASA OMNIWeb database. The dawn-dusk electric field component was computed as

$$E_y = -V_{\rm sw} B_z, \tag{1}$$

where $V_{\rm sw}$ ($\mathrm{km\,s^{-1}}$) is the solar wind speed and B_z (nT) is the north–south IMF component in GSM coordinates.

Physically, E_y represents the convection electric field imposed at the magnetopause. A sustained southward B_z enhances magnetic reconnection, increasing magnetospheric convection and enabling penetration of electric fields to low latitudes. For consistency with ionospheric electrodynamic units, E_y was converted to $\mathrm{mV\,m^{-1}}$. Placeholder values were excluded prior to computation. Solar wind coupling functions and sustained southward IMF intervals were used to identify periods of enhanced magnetosphere–ionosphere energy transfer that typically precede PPEF signatures (Gonzalez et al., 1994; Fejer et al., 2010).

2.2 Thermospheric Composition Data (O/N_2 Ratio)

Thermospheric composition was examined using the atomic oxygen to molecular nitrogen ratio (O/N_2) derived from the Global Ultraviolet Imager (GUVI) instrument onboard the TIMED satellite mission. GUVI measures far-ultraviolet (FUV) airglow emissions, from which column O/N_2 ratios are retrieved as proxies for thermospheric neutral composition variability. The O/N_2 dataset covering 10-12 November 2025 was obtained from the NASA GUVI archive, corresponding to pre-storm, storm, and recovery phases. The data have a spatial resolution of approximately $1^\circ \times 1^\circ$ in latitude and longitude. Storm-time O/N_2 variations were analyzed relative to quiet-day reference conditions. Physically, depletion in O/N_2 indicates thermospheric upwelling caused by auroral Joule heating, which increases molecular nitrogen abundance at F-region heights. Since N_2 enhances recombination through

$$O^+ + N_2 \rightarrow NO^+ + N,$$

reduced O/N_2 leads to plasma density depletion and negative TEC responses during recovery phases. Thus, this dataset provides critical context for interpreting DDEF-related composition-driven effects.

2.3 Ionospheric TEC Data

To quantify ionospheric storm responses, dual-frequency GNSS observations from selected stations (Table 1) were used to estimate TEC variations associated with PPEF- and DDEF-driven plasma transport. RINEX files were obtained from the International GNSS Service (IGS) and UNAVCO archives. Slant TEC (STEC) was estimated from dual-frequency carrier phase and pseudo-range measurements using the dispersive nature of the ionosphere:

$$\mathrm{STEC} = \frac{f_1^2 f_2^2}{40.3(f_1^2 - f_2^2)}(L_1 - L_2), \tag{2}$$

Table 1: Geographic details of GNSS stations used in the study.

Country	Station Name	IGS Code	Latitude	Longitude
Brazil	Belem	BELE	1.408°S	48.46°W
Ecuador	Quito	QUI4	0.18°S	78.47°W
Brazil	Boa Vista	BOAV	2.82°N	60.67°W
Indonesia	Cibubur	BAKO	6.38°S	106.91°E
Papua New Guinea	Lae1	LAE1	6.67°S	146.67°E
Nauru	Nauru	NAU2	0.523°S	166.916°E

where f_1 and f_2 are GNSS frequencies and L_1, L_2 are phase measurements (Archana et al., 2023b). The physical meaning is straightforward: the ionosphere introduces a frequency-dependent delay proportional to integrated electron density along the ray path. Vertical TEC (VTEC) was derived using a single-layer mapping function:

$$\mathrm{VTEC} = \mathrm{STEC} \times \cos z', \tag{3}$$

where z' is the zenith angle at the assumed ionospheric shell height of 350 km. This thin-shell approximation represents the effective altitude of maximum electron density in the F_2 region. Only satellite elevation angles above 30° were used to minimize multipath errors. Cycle-slip detection and receiver bias corrections followed standard GNSS processing techniques. Storm perturbations were defined as

$$\Delta\mathrm{TEC} = \mathrm{TEC}_{\mathrm{storm}} - \mathrm{TEC}_{\mathrm{quiet}}, \tag{4}$$

where the quiet reference is the mean of adjacent geomagnetically quiet days.

2.4 Magnetometer Observations

Ground-based magnetometer data were used to investigate storm-time current systems and equatorial electrodynamic responses. High-resolution magnetic field data from INTERMAGNET stations in South America and Africa were analyzed. The horizontal magnetic field (H-component) variations served as a proxy for EEJ intensity. Physically, the EEJ is an eastward current flowing in the daytime E-region, producing an enhancement in the horizontal magnetic field near the magnetic equator. Differential analysis between equatorial and off-equatorial stations isolates EEJ strength:

$$\Delta H_{\mathrm{EEJ}} = H_{\mathrm{eq}} - H_{\mathrm{off}}, \tag{5}$$

where H_{eq} and H_{off} are the horizontal components at equatorial and reference stations, respectively.

Stations included:

- Tatuoca (TTB), Brazil (1.20°S, 48.50°W), near the magnetic equator.
- Vassouras (VSS), Brazil (22.40°S, 43.70°W), off-equatorial reference.

These measurements enabled precise characterization of both the prompt and delayed responses of the equatorial ionosphere to geomagnetic storm forcing.

2.5 Derivation of Electric Field Drivers

Rapid southward IMF B_z turnings were identified as triggers of PPEFs. The interplanetary electric field was computed using

$$E_y = -V_{\mathrm{sw}} B_z. \tag{6}$$

Cross-correlation analysis between E_y, ΔTEC, and ΔH_{EEJ} was performed to evaluate temporal coupling. PPEFs were identified by near-simultaneous enhancements in E_y, upward plasma drift signatures (TEC uplift), and intensified EEJ within minutes to hours of IMF southward turnings. DDEFs were diagnosed from delayed, long-duration signatures characterized by:

- Sustained westward electric field signatures inferred from EEJ weakening,
- Suppression of the equatorial prereversal enhancement (PRE),
- Prolonged negative ΔTEC during recovery phase,
- Temporal delay of 3–6 hours relative to IMF variations.

Physically, PPEFs represent direct magnetospheric forcing transmitted rapidly to low latitudes, whereas DDEFs reflect the slower thermospheric wind-driven dynamo response. The contrasting time scales and polarity signatures allow separation of these two electrodynamic mechanisms.

3 Results and Discussion

3.1 Ionospheric TEC Response

Figure 1 shows the ionospheric response to the November 2025 geomagnetic storm over Africa, South America, and Southeast Asia, assessed using GNSS-derived vertical total electron content (VTEC) from six stations: BAKO, BELE, BOAV, LAE1, NAU2, and QUI4. The observations reveal a classical two-phase storm-time behavior characterized by positive ionospheric storm effects during the main phase and negative effects during recovery. Such storm-time dual behavior has been widely reported in equatorial and low-latitude studies (Mannucci and Tsurutani, 2017; Fejer et al., 2024). Thus significant day-to-day variability was observed between 10–12 November 2025. During the storm main phase (11 November), pronounced TEC enhancements were observed, particularly during daytime hours at equatorial stations, and around the pre-reversal enhancement (PRE) interval in the evening sector. Positive ΔTEC indicates significant plasma uplift consistent with eastward PPEF forcing. The eastward electric field produces an upward $\mathbf{E} \times \mathbf{B}$ drift given by

$$\mathbf{V}_d = \frac{\mathbf{E} \times \mathbf{B}}{B^2}, \tag{7}$$

which lifts the F-region plasma to higher altitudes where neutral density is lower and recombination rates decrease. This upward transport enhances electron density and intensifies the equatorial fountain effect, redistributing plasma toward the low-latitude crests of the equatorial ionization anomaly (EIA). In contrast, the post-storm recovery phase exhibits sustained TEC reductions relative to quiet-time baselines. These negative storm-phase signatures reflect westward-directed DDEFs generated by thermospheric wind modifications following high-latitude Joule heating and enhanced energy deposition. The depletion is most pronounced during nighttime and early morning hours, consistent with reduced upward plasma transport and enhanced chemical recombination (Zhang, 2025).

The spatial coherence of TEC enhancement across longitudinal sectors confirms large-scale magnetosphere–ionosphere coupling. However, the magnitude of enhancement differs by longitude, consistent with earlier findings that storm-time ionospheric responses exhibit strong longitudinal dependence due to background electrodynamics, magnetic declination, and thermospheric wind structures (Bojilova and Mukhtarov, 2024; Nair et al., 2026). The QUI4 station did not record storm-time TEC, highlighting observational gaps in certain longitude sectors. In contrast, the

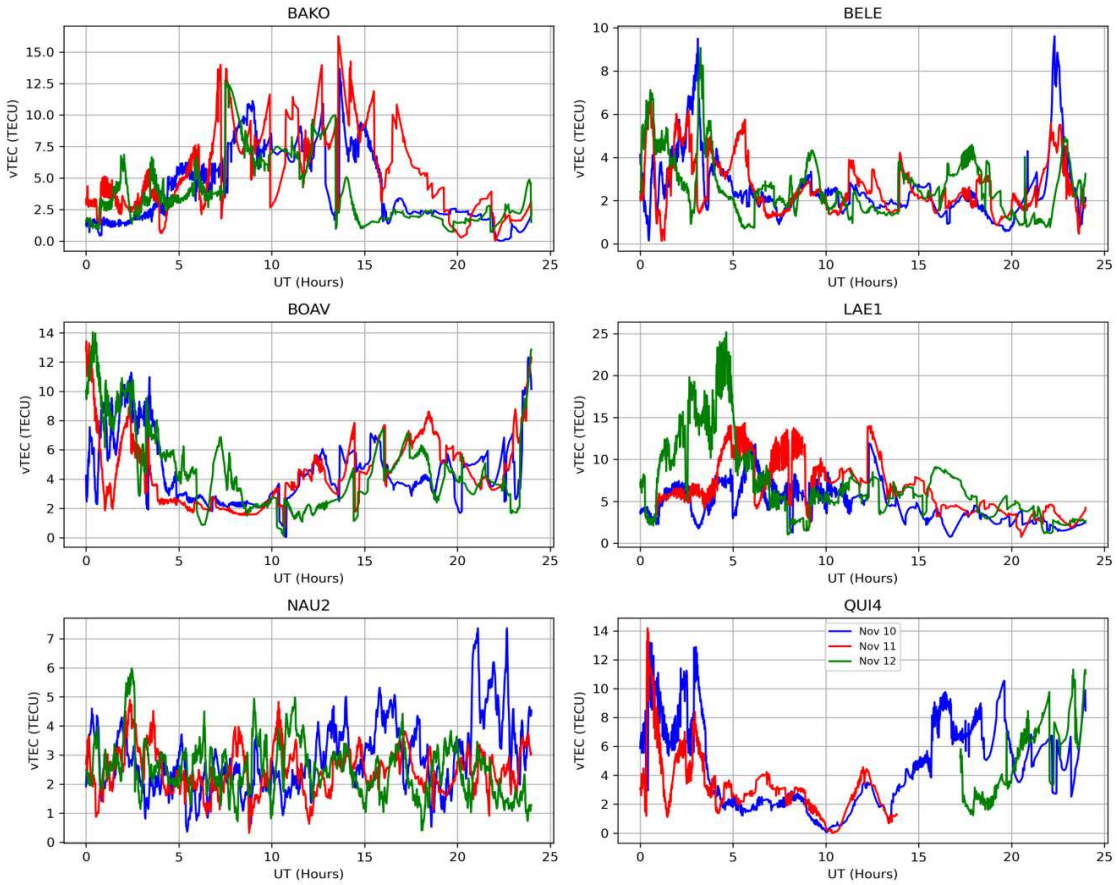


Figure 1: vTEC variations at six GNSS stations (BAKO, BELE, BOAV, LAE1, NAU2, QUI4) during November 10 -12, 2025. Storm-day (Nov 11, red) is compared with pre-storm (Nov 10, blue) and post-storm (Nov 12, green) reference days to highlight ionospheric perturbations.

recovery phase (12 November) shows sustained TEC depletion relative to quiet-time conditions. These negative storm signatures are characteristic of disturbance dynamo electric field (DDEF) dominance. DDEFs arise from storm-driven thermospheric circulation changes caused by auroral Joule heating and enhanced energy deposition (Fuller-Rowell et al., 1994). The delayed onset and longer persistence of TEC depletion align with previously documented thermospheric wind dynamo response timescales of several hours. The ionospheric response varied across longitudinal sectors. The Asian sector stations (BAKO, LAE1) showed stronger storm-time TEC enhancement compared to some American and Pacific sector stations. This longitudinal dependence can be attributed to, local time of storm onset, background ionospheric conditions, magnetic declination differences, and Sector-dependent thermospheric wind patterns. Such variability highlights the coupling between magnetospheric forcing and regional electrodynamics.

3.2 TEC Perturbations (ΔTEC)

Storm-induced ionospheric variability was quantified using

$$\Delta\text{TEC} = \text{TEC}_{\text{storm}} - \text{TEC}_{\text{quiet}}, \tag{8}$$

where the quiet-time reference is defined as the average TEC of November 10 and 12. Figure 2 presents ΔTEC for all six stations. Positive ΔTEC peaks align temporally with sudden southward IMF B_z turnings and enhanced interplanetary electric field E_y, confirming the rapid penetration of PPEFs to low latitudes. Peak values occurred during local daytime and evening hours, correspond-

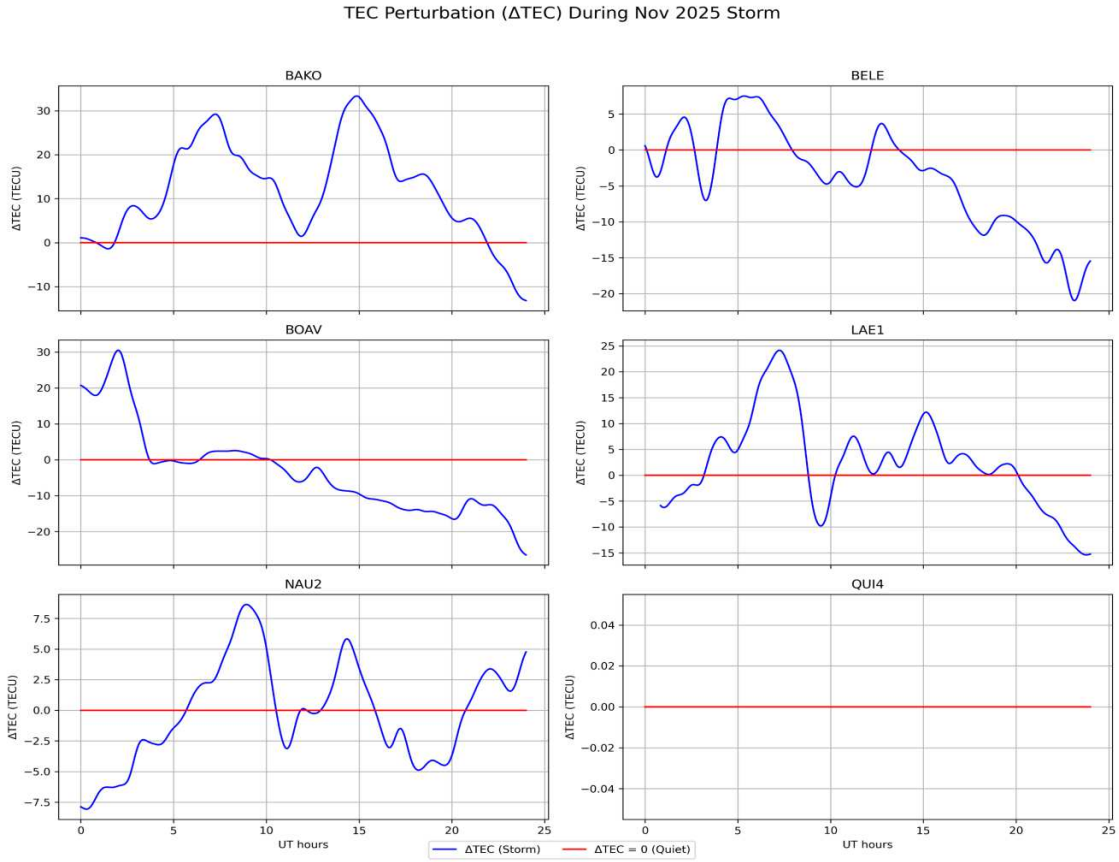


Figure 2: ΔTEC observed at six low-latitude GNSS stations at geomagnetic storm, highlights storm-induced ionospheric variability, with positive values refers TEC enhancements and negative values refers TEC depletions. QUI4 station shows no storm-time data.

ing to enhanced vertical drifts and strengthening of the plasma fountain mechanism. Negative ΔTEC during the recovery phase reflects DDEF-dominated processes. Westward electric field forcing reduces upward drift, while increased molecular nitrogen concentration enhances recombination in the F-region. The characteristic 3-6 hour delay between the storm main phase and TEC depletion corresponds to thermospheric wind propagation and dynamo response timescales. Thus, ΔTEC provides a clear temporal diagnostic separating prompt magnetospheric forcing (PPEF) from delayed thermospheric dynamo effects (DDEF).

3.3 Geomagnetic Field Variations

Ground-based magnetometer observations provide complementary insight into storm-time electrodynamics. Figure 3 and Figure 4 display variations of the X (northward), Y (eastward), Z (vertical), and total field F components at VSS and TTB stations respectively. Prior to the storm, the Z-component was largely sable, but during the storm, it exhibited significant variations (Data et al., 2026). Therefore, an abrupt excursions in the X and Y components were observed, reflecting EEJ intensification and PPEF penetration as shown in figure 3. Rapid EEJ enhancement indicates strengthened eastward electric fields in the E-region, directly linked to the near-instantaneous plasma uplift observed in ΔTEC. A pronounced decrease in the horizontal component X is ob-

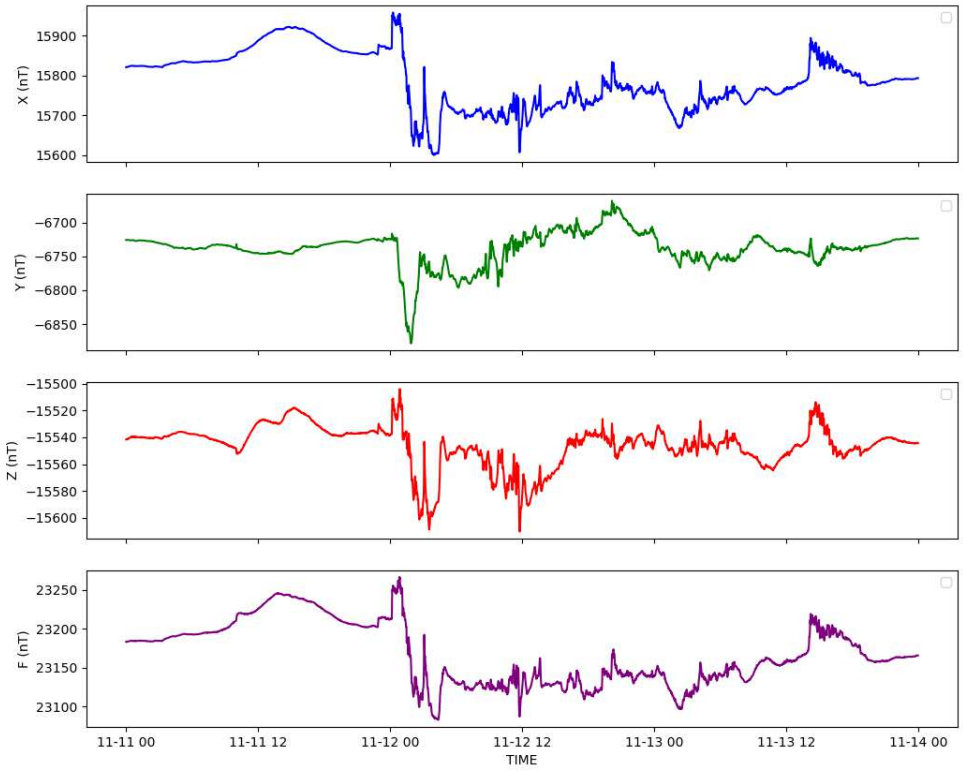


Figure 3: Geomagnetic field variations at the VSS station, Components X (northward), Y (eastward), Z (vertical), and total field F (nT) are shown to illustrate storm-time geomagnetic perturbations.

served during the storm main phase, accompanied by significant perturbations in Y and Z, while the total magnetic field F exhibits a marked negative excursion. The reduction in X reflects the intensification of the storm-time ring current, as the disturbance field ΔH (approximated by ΔX at low latitudes) is directly proportional to ring current strength and closely related to the Dst index. Concurrent fluctuations in Y indicate enhanced ionospheric and asymmetric magnetospheric current systems, whereas strong deviations in Z suggest variability in the equatorial electrojet, penetration electric fields, and intensified magnetosphere–ionosphere coupling. The depression in F

represents the integrated effect of these disturbed current systems, and its gradual recovery signifies ring current decay and magnetospheric relaxation during the recovery phase. During the recovery phase, a gradual decrease in EEJ intensity was observed, accompanied by weaker variations in Z and F components. These signatures are consistent with westward DDEF-driven electric fields. The delayed geomagnetic response parallels TEC depletion, reinforcing the coupled behavior of geomagnetic currents and ionospheric plasma transport.

The geomagnetic field variations recorded at the TTB station show a relatively quiet interval on 11–11 with smooth diurnal trends in all components, followed by a pronounced disturbance beginning around 11–12 00 UT as shown in figure 4. The northward component X exhibits a sudden positive excursion immediately followed by a sharp decrease of nearly 300 nT, indicating the onset of a geomagnetic disturbance. Similarly, the eastward component Y shows a rapid negative deflection exceeding 100 nT, while the vertical component Z undergoes strong fluctuations with a marked decrease, reflecting significant perturbations in the magnetospheric and ionospheric current systems. The total field F correspondingly drops by more than 100 nT, confirming an overall weak-

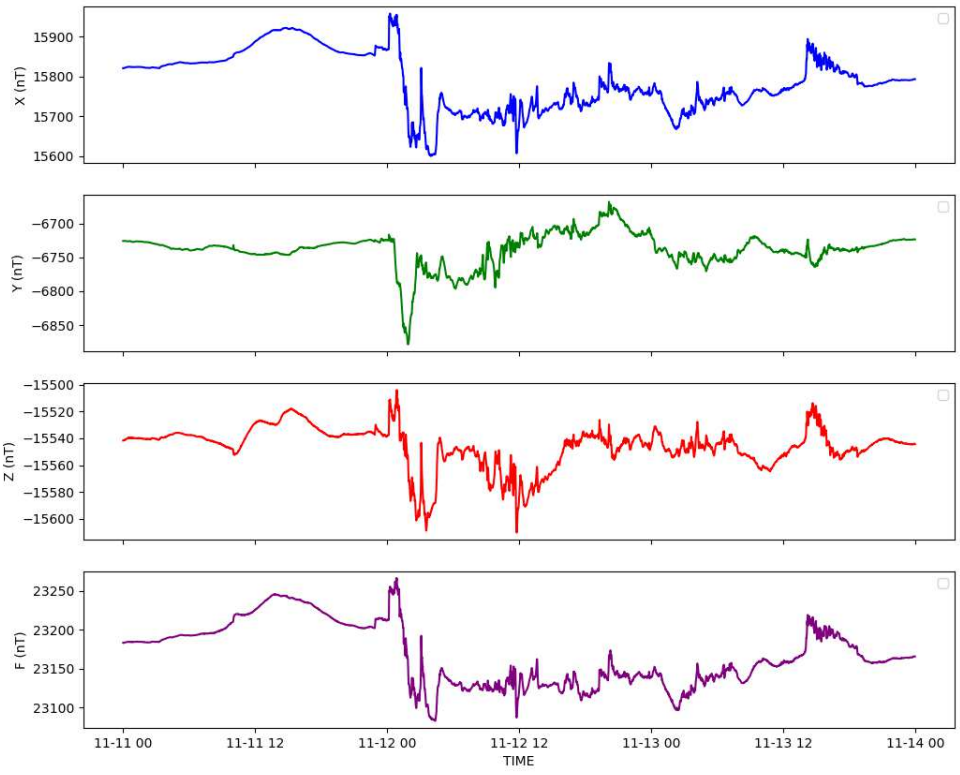


Figure 4: Geomagnetic field variations at the TTB station, Components X (northward), Y (eastward), Z (vertical), and total field F (nT) are shown to illustrate storm-time geomagnetic perturbations.

ening of the magnetic field intensity during the main phase of the disturbance. After the sudden impulse and main phase, enhanced irregular fluctuations persist through 11–12 and into 11–13,

suggesting continuing substorm activity and recovery processes. By late 11–13, the components gradually return toward their pre-disturbance levels, indicating the recovery phase of the geomagnetic event (Seba and Nigussie, 2016). Overall, the simultaneous and coherent variations in X, Y, Z, and F are characteristic of a moderate geomagnetic storm with a clear sudden commencement, main phase depression, and gradual recovery.

3.4 Solar Wind and Geomagnetic Indices

Solar wind and interplanetary conditions act as primary drivers of low-latitude ionospheric responses. Figure 5 illustrates variations in IMF components (B_x, B_y, B_z), solar wind speed (V_{sw}), interplanetary electric field (E_y), and geomagnetic indices (Dst and Kp) over November 11–13. Storm onset is marked by sustained southward IMF B_z and elevated E_y, driving eastward PPEFs

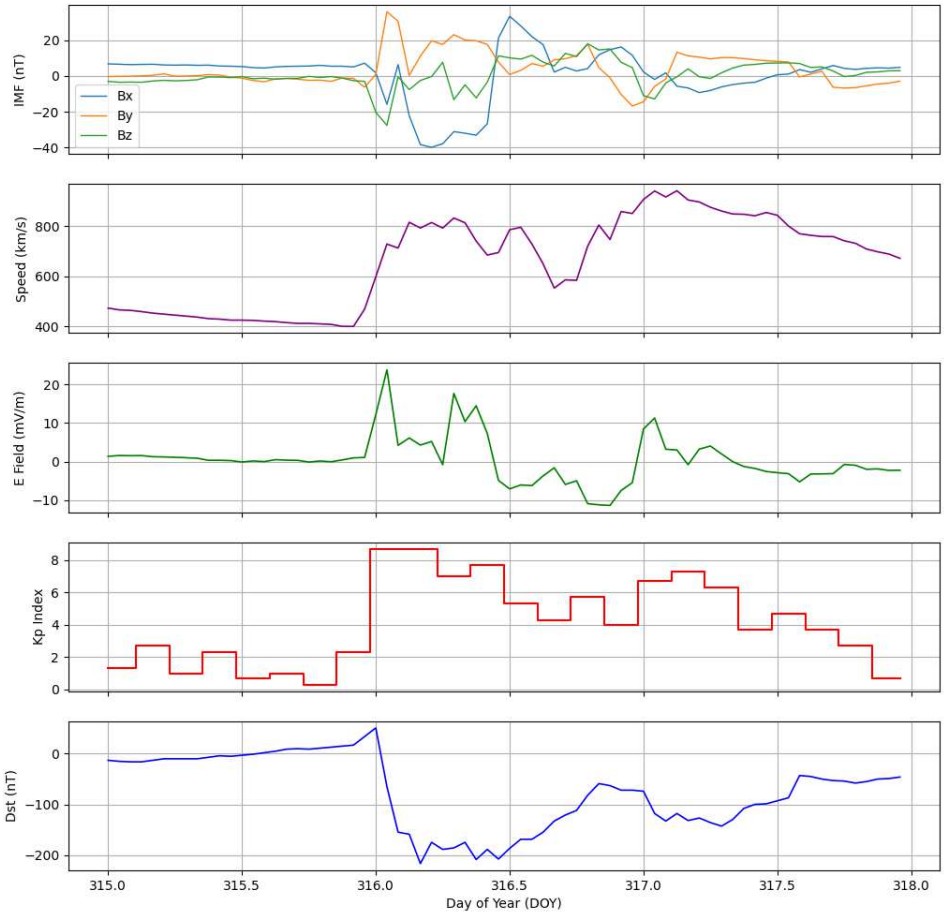


Figure 5: Variations of IMF components (B_x, B_y, B_z), solar wind speed (Vsw), interplanetary electric field (E_y), and geomagnetic indices (Dst and Kp) during geomagnetic storm, highlighting solar wind forcing and corresponding geomagnetic activity.

and consequent TEC enhancement. Increased V_{sw} amplifies magnetospheric energy transfer, reflected in a sharp Dst depression and elevated Kp values. The temporal alignment between southward B_z, peak E_y, and maximum ΔTEC confirms direct solar wind–ionosphere coupling. During the recovery phase, gradual Dst and Kp recovery and declining E_y correspond to westward DDEF forcing and TEC depletion. This transition reflects the shift from direct magnetospheric control to thermospheric dynamo dominance.

3.5 Thermospheric Composition: O/N_2 Ratio

Thermospheric composition variations derived from GUVI O/N_2 observations provide critical insight into the role of neutral atmosphere dynamics in regulating storm-time ionospheric responses. Figure 6 presents O/N_2 ratio variations for November 10-12. During the storm day (November 11), a reduction in O/N_2 is observed relative to quiet days, indicating enhanced molecular nitrogen abundance due to thermospheric upwelling. Reduced O/N_2 accelerates F-region recombination,

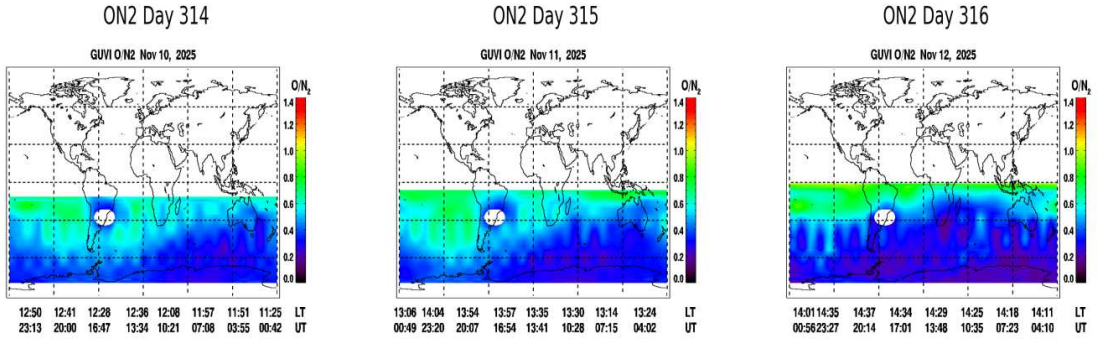


Figure 6: Variation of the O/N_2 ratio during November, 2025 storm. The plot highlights the storm-induced enhancements and depletions in thermospheric composition, isolating storm-time ionospheric responses from background diurnal variations.

contributing to negative ΔTEC during the recovery phase. The combined analysis of O/N_2, ΔTEC, and EEJ variations demonstrates the coupled roles of electrodynamic forcing and thermospheric composition changes in controlling low-latitude storm-time ionospheric responses. Enhanced plasma structuring and TEC gradients observed in the post-sunset sector suggest favorable conditions for equatorial plasma bubble generation and scintillation development. Overall, the combined TEC, magnetometer, solar wind, and thermospheric observations confirm the sequential and competing roles of PPEFs and DDEFs during the November 2025 storm. The results align with established theoretical and observational frameworks of storm-time electrodynamics (Tsurutani, 2008), while extending understanding to underrepresented African and multi-longitude sectors, and thus the maps offer an understanding of how storms alter the neutral composition of the thermosphere, which is a key element affecting fluctuations in ionospheric electron density (Data et al., 2026). Overall, the thermospheric composition analysis demonstrates that storm-time ionospheric variability cannot be explained solely by electrodynamic forcing. Instead, it results from the coupled interaction between magnetospheric drivers, thermospheric wind circulation, and chemical recombination processes. The November 2025 storm clearly illustrates how composition-driven plasma loss reinforces dynamo-induced electric field effects, producing prolonged negative storm phases across low-latitude regions.

4 Conclusion

The November 2025 geomagnetic storm produced pronounced ionospheric disturbances across equatorial and low-latitude regions of Africa, South America, and Southeast Asia. Storm-time responses were governed by the combined action of PPEFs and DDEFs. Rapid TEC enhancement and EEJ intensification during the main phase are consistent with eastward PPEF-driven upward plasma drift and strengthening of the EIA crests. The close temporal correspondence between southward IMF B_z, enhanced E_y, and abrupt TEC increases confirms direct solar wind control of low-latitude electrodynamics. During the recovery phase, delayed TEC depletion, weakened EEJ signatures, and suppression of the PRE indicate dominance of westward DDEFs generated by storm-driven thermospheric circulation. These delayed responses reflect the time required for high-latitude energy deposition and Joule heating to modify global neutral wind systems, reducing equatorial fountain efficiency. Regional longitudinal variability was evident and influenced by magnetic declination, background ionospheric conditions, and electrodynamic coupling efficiency. Despite observational limitations in parts of Africa, the integration of GNSS TEC and magnetometer data demonstrates the effectiveness of multi-instrument diagnostics for resolving storm-time electrodynamic processes. The observed TEC perturbations have direct implications for GNSS navigation accuracy, satellite communications, and space-based infrastructure reliability in equatorial regions. Integrating solar wind, geomagnetic, thermospheric, and ionospheric observations is essential for disentangling PPEF and DDEF contributions and improving storm-time forecasting capability. Overall, this study confirms that storm-time equatorial ionospheric variability is governed by the competing and time-dependent interplay between rapid penetration electric fields and delayed disturbance dynamo processes. The findings contribute to improved understanding of low-latitude space weather dynamics and have direct implications for GNSS positioning accuracy, satellite communication reliability, and forecasting of equatorial ionospheric disturbances. Future studies incorporating ionosonde data, incoherent scatter radar measurements, and physics-based modeling would further enhance the quantitative separation of penetration and dynamo contributions during intense geomagnetic events.

Acknowledgement

The authors acknowledge that GNSS, magnetometer, solar wind, thermospheric, and geomagnetic index data were obtained from publicly available data centers, including IGS, INTERMAGNET, GUVI, and OMNIWeb. The efforts of these organizations in providing high-quality datasets are gratefully acknowledged.

Funding

This work did not receive any specific grant from funding agencies in the public, commercial, or not-for-profit sectors.

Data Availability

Processed data supporting the findings of this study are available from the corresponding author upon reasonable request.

Author Contributions

Efrem A. (http://orcid.org/0009-0006-3668-5445) conceptualized the study, developed the research methodology, conducted data acquisition and processing, performed analysis and visualization, and prepared the original manuscript draft. **Emmanuel D. Sulungu** (http://orcid.org/0000-0002-3234-0953) contributed to study conceptualization, interpretation of the results, and overall supervision of the research work. **Gebre K.** (http://orcid.org/0000-0003-2253-5842) contributed to manuscript review, editing, and writing improvement. All authors actively participated in revising the manuscript, approved the final version, and take responsibility for the accuracy and integrity of the work.

References

R. K. Archana, K. Arora, and N. Nagarajan. Prompt penetration effects on equatorial electrojet from the indian sector. *Earth, Planets and Space*, 75, 2023a.

RK Archana, Kusumita Arora, and Nandini Nagarajan. Prompt penetration effects on equatorial electrojet from the indian sector. *Earth, Planets and Space*, 75(1):122, 2023b.

D. et al. Bai. The poleward shift of the equatorial ionization anomaly during the main phase of the superstorm on 10 may 2024. *Remote Sensing (Basel)*, 17, 2025.

R. Bojilova and P. Mukhtarov. Seasonal features of the ionospheric total electron content response at low latitudes during three selected geomagnetic storms. *Atmosphere (Basel)*, 15, 2024.

R. K. Burton, R. L. McPherron, and C. T. Russell. An empirical relationship between interplanetary conditions and dst. *Journal of Geophysical Research*, 80:4204–4214, 1975.

Y. et al. Chen. The extreme depletion of ionospheric electron density and its hemispheric asymmetry during the may 2024 storm. *National Science Review*, 12, 2025.

L. A. Daglis, R. M. Thorne, W. Baumjohann, and S. Orsini. The terrestrial ring current: Origin, formation, and decay. *Reviews of Geophysics*, 37:407–438, 1999.

E. Data. Variation of total electron content over may 10–13 2024 geomagnetic super storm in south africa. *International Journal of Astrophysics and Space Science*, 13:21–35, 2025.

E. A. Data, D. A. Terefe, S. G. Gutulo, et al. Dynamics of equatorial and low-latitude tec fluctuations during the april 2023 geomagnetic storm. *Kinematics and Physics of Celestial Bodies*, 42 (1):24–39, 2026. doi: 10.3103/S0884591326010034.

J. M. Dow, R. E. Neilan, and C. Rizos. The international gnss service in a changing landscape of global navigation satellite systems. *Journal of Geodesy*, 83:191–198, 2009.

J. W. Dungey. Interplanetary magnetic field and the auroral zones. *Physical Review Letters*, 6(2), 1961.

B. G. Fejer, L. A. Navarro, and D. Chakrabarty. Recent results and outstanding questions on the response of the electrodynamics of the low latitude ionosphere to solar wind and magnetospheric disturbances. *Frontiers in Astronomy and Space Sciences*, 11, 2024.

BG Fejer, ME Olson, JL Chau, Claudia Stolle, Hermann Lühr, LP Goncharenko, K Yumoto, and T Nagatsuma. Lunar-dependent equatorial ionospheric electrodynamic effects during sudden stratospheric warmings. *Journal of Geophysical Research: Space Physics*, 115(A8), 2010.

TJ Fuller-Rowell, MV Codrescu, RJ Moffett, and S Quegan. Response of the thermosphere and ionosphere to geomagnetic storms. *Journal of Geophysical Research: Space Physics*, 99(A3): 3893–3914, 1994.

W. D. Gonzalez, J. A. Joselyn, Y. Kamide, H. W. Kroehl, G. Rostoker, B. T. Tsurutani, and V. M. Vasyliunas. What is a geomagnetic storm? *Journal of Geophysical Research: Space Physics*, 99: 5771–5792, 1994.

F. Han, S. A. Cummer, J. Li, and G. Lu. Daytime ionospheric d region sharpness derived from vlf radio atmospherics. *Journal of Geophysical Research: Space Physics*, 116, 2011.

T. Kikuchi and K. K. Hashimoto. Transmission of the electric fields to the low latitude ionosphere in the magnetosphere-ionosphere current circuit. *Geoscience Letters*, 3, 2016.

G. Lu, L. Goncharenko, M. J. Nicolls, A. Maute, A. Coster, and L. J. Paxton. Ionospheric and thermospheric variations associated with prompt penetration electric fields. *Journal of Geophysical Research: Space Physics*, 117, 2012.

X. Luo, E. Aa, X. Wang, and B. Luo. Strong longitudinal and latitudinal differences of ionospheric responses in north american and european sectors during the 10–11 october 2024 geomagnetic storm. *Remote Sensing (Basel)*, 18:256, 2026.

R. Malik, S. Sarkar, S. Mukherjee, and A. K. Gwal. Study of ionospheric variability during geomagnetic storms. 14, 2010.

A. J. Mannucci and B. T. Tsurutani. Ionosphere and thermosphere responses to extreme geomagnetic storms. *Extreme Events in Geospace: Origins, Predictability, and Consequences*, pages 493–511, 2017.

R. R. Meier, G. Crowley, D. J. Strickland, A. B. Christensen, L. J. Paxton, D. Morrison, and C. L. Hackert. First look at the 20 november 2003 superstorm with timed/guvi: Comparisons with a thermospheric global circulation model. *Journal of Geophysical Research: Space Physics*, 110, 2005.

Michel Menvielle. The contribution of a geophysical data service: The international service of geomagnetic indices. *Data Science Journal*, 12:WDS27–WDS31, 2013.

S. P. et al. Moraes-Santos. Influence of solar wind high-speed streams on the brazilian low-latitude ionosphere during the descending phase of solar cycle 24. *Space Weather*, 22, 2024.

Remya S. Nair, K. Unnikrishnan, Smitha V. Thampi, and Sreekumar Haridas. Longitudinal variation in the ionospheric responses to two successive geomagnetic storms in early solar cycle 25. *Advances in Space Research*, 77(4):5222–5235, 2026. ISSN 0273-1177. doi: 10.1016/j.asr.2025.12.037. URL https://www.sciencedirect.com/science/article/pii/S0273117725014474.

K. S. et al. Paul. Effects of the mother's day superstorm (10–11 may 2024) over the global ionosphere. *Remote Sensing (Basel)*, 17, 2025.

V. Pierrard, T. G. W. Verhulst, J. M. Chevalier, N. Bergeot, and A. Winant. Effects of the geomagnetic superstorms of 10–11 may 2024 and 7–11 october 2024 on the ionosphere and plasmasphere. *Atmosphere (Basel)*, 16, 2025.

S. et al. Pulinets. Ionospheric response to the geomagnetic storm of 12–14 november 2025, based on multi-parameter analysis of data from the laert topside sounder. *Atmosphere (Basel)*, 17:150, 2026.

Norbert Sckopke. A general relation between the energy of trapped particles and the disturbance field near the earth. *Journal of Geophysical Research*, 71(13):3125–3130, 1966.

E. B. Seba and M. Nigussie. Investigating the effect of geomagnetic storm and equatorial electrojet on equatorial ionospheric irregularity over east african sector. *Advances in Space Research*, 58: 1708–1719, 2016.

E. D. Sulungu. Performance of iri 2016 model in predicting total electron content (tec) compared with gps-tec over east africa during 2019–2021. *Scientific Reports*, 14, 2024.

B. T. et al. Tsurutani. Prompt penetration electric fields (ppefs) and their ionospheric effects during the great magnetic storm of 30–31 october 2003. *Journal of Geophysical Research: Space Physics*, 113, 2008.

S. Tulasi Ram, B. Nilam, N. Balan, Q. Zhang, K. Shiokawa, D. Chakrabarty, Z. Xing, K. Venkatesh, B. Veenadhari, and A. Yoshikawa. Three different episodes of prompt equatorial electric field perturbations under steady southward imf bz during st. patrick's day storm. *Journal of Geophysical Research: Space Physics*, 124:10428–10443, 2019.

I. Venugopal, S. V. Thampi, and A. Bhaskar. Electrodynamic forcing of the duskside ionosphere and the super fountain effect during the superstorm of may 10–11 2024. *Scientific Reports*, 15, 2025.

E. Yizengaw. Ionospheric dynamics and their strong longitudinal dependences. *Ionosphere Dynamics and Applications*, pages 401–419, 2021.

R. Zhang, L. Liu, X. Yue, J. Zhang, N. Zhang, Y. Chen, H. Le, and W. Li. The penetration electric fields during the 10 may 2024 superstorm observed by isrs over sanya and jicamarca. *Geophysical Research Letters*, 52, 2025.

Z. et al. Zhang. The magnetosphere-ionosphere-ground responses to the may 2024 super solar storm. *Space Weather*, 23, 2025.